Volume 13
Number 6
23 March 2026
Pages 2599–3130

Materials Horizons

rsc.li/materials-horizons

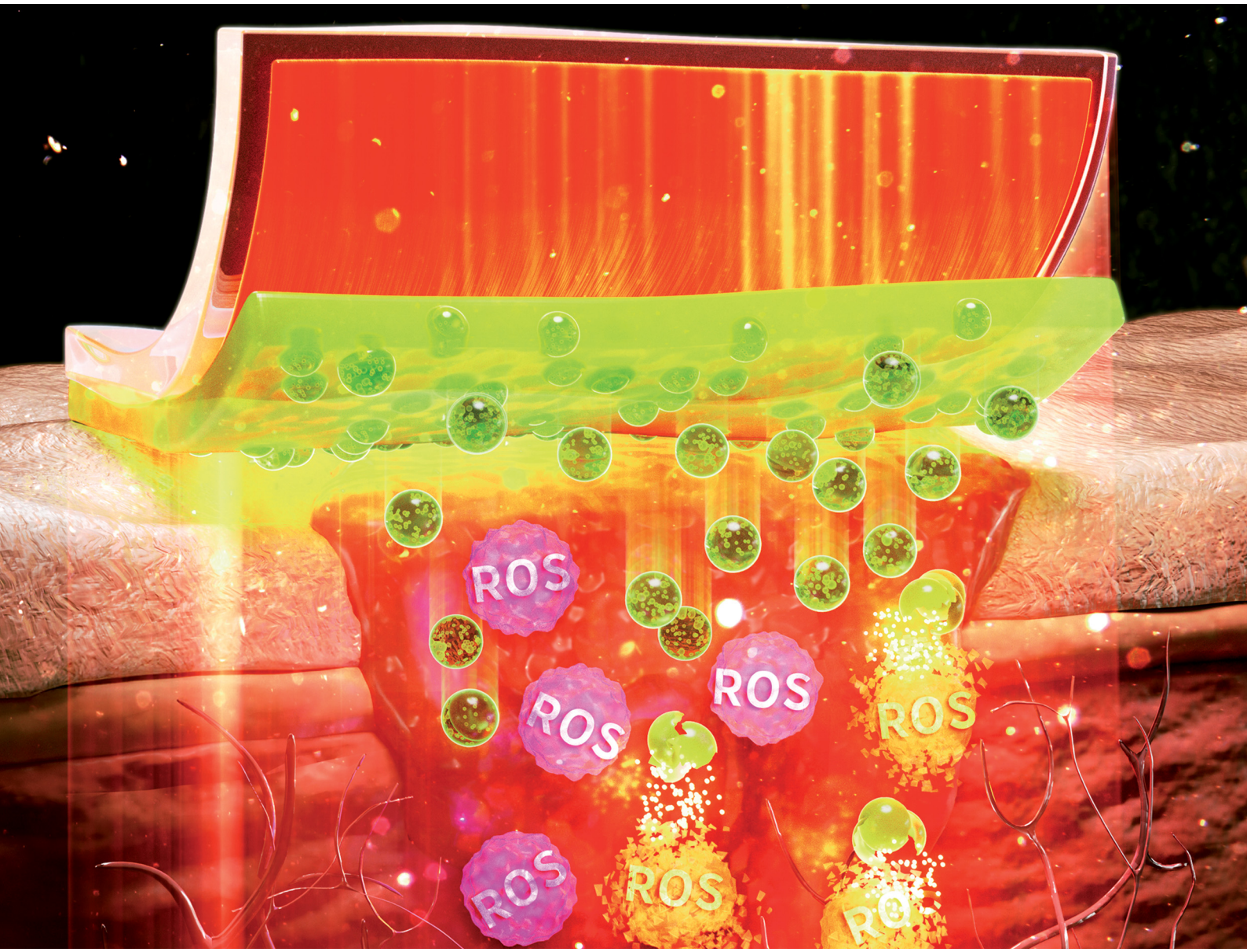

ISSN 2051-6347

COMMUNICATION

Yongmin Jeon, Chan-Su Park, Daekyung Sung, Kyung Cheol Choi *et al.*
A self-regulating wearable OLED patch for accelerated wound healing *via* photobiomodulation-triggered drug delivery

ROYAL SOCIETY OF CHEMISTRY

Materials Horizons

ROYAL SOCIETY OF CHEMISTRY

COMMUNICATION

View Article Online
View Journal | View Issue

Cite this: *Mater. Horiz.*, 2026, 13, 2786

Received 8th November 2025,
Accepted 21st January 2026

DOI: 10.1039/d5mh02129d

rsc.li/materials-horizons

A self-regulating wearable OLED patch for accelerated wound healing *via* photobiomodulation-triggered drug delivery

Hyejeong Yeon,†[a] Sohyeon Yu,†[bc] Minhyeok Lee,†[d] Sangwoo Kim,†[bc] Yongjin Park,[a] Hye-Ryung Choi,[e] Won Il Choi,[b] Chang-Hun Huh,[e] Yongmin Jeon,*[f] Chan-Su Park,*[d] Daekyung Sung*[b] and Kyung Cheol Choi*[a]

The development of therapies that dynamically respond to the wound microenvironment is essential to overcome the limitations of conventional monotherapies. We present a wearable patch that self-regulates reactive oxygen species (ROS) to accelerate wound healing. This flexible organic light-emitting diode (OLED) patch conforms to the wound, delivering narrow 630 nm peak light at an irradiance of 5 mW cm^{-2} for photobiomodulation (PBM). The patch activates healing directly *via* PBM, and the consequently induced ROS serve as a therapeutic trigger. This ROS trigger stimulates ROS-responsive nanoparticles to release antioxidant drugs, which neutralize excess ROS. We confirmed a dose-dependent additive effect across 2–8 J cm^{-2}, with 6 J cm^{-2} being the most effective. This combination therapy significantly accelerated wound closure and promoted superior tissue regeneration, including robust skin barrier reconstruction and mature vessel stabilization. This OLED patch introduces a next-generation phototherapy, transforming signals into therapeutic triggers for advanced combination treatments.

New concepts

Conventional photobiomodulation (PBM) and drug delivery systems (DDS) have independently advanced wound therapy but remain limited by passive integration and the lack of active interaction between light and drugs. In this work, we introduce a self-regulating wearable OLED patch that establishes an active phototherapy–drug delivery feedback loop. The flexible red OLED provides a uniform 630 nm emission for PBM, directly stimulating tissue regeneration, while the mild reactive oxygen species (ROS) generated during PBM act as endogenous biochemical triggers to activate ROS-responsive nanoparticles for on-demand drug release. This dual functionality transforms PBM light from a passive energy source into a dynamic therapeutic signal transducer, enabling precise, self-regulated modulation of the wound microenvironment. Unlike previous LED-based systems, the OLED's conformability, thermal stability, and wavelength specificity allow continuous, localized treatment with minimal irritation. Furthermore, the efficacy of this feedback-based therapy was validated in both *in vitro* and *in vivo* models, demonstrating rapid and stable wound regeneration along with mature skin barrier reconstruction. This concept introduces a paradigm shift in combination therapy—from co-existing modalities to a mutually interactive system—offering a new route for intelligent, feedback-driven phototherapy that can be extended to diverse biomedical applications beyond wound healing.

Introduction

The skin, the body's largest organ, serves as the primary barrier protecting the body from external insults. When this barrier is compromised by injury or disease, the tissue becomes vulnerable to secondary damage such as infection and scarring, necessitating accelerated healing.[1,2] Failure in this process extends beyond simple discomfort, degrading a patient's quality of life and imposing significant economic and social burdens on both individuals and the healthcare system. To address this challenge, extensive research has focused on accelerating wound healing through the application of growth factors such as the epidermal growth factor (EGF) and fibroblast growth factor (FGF), naturally derived drugs like *Centella asiatica* (CA), and chemically synthesized compounds.[3,4] However, the conventional topical application of these substances suffers from fundamental limitations, including poor delivery efficiency to the therapeutic site and the necessity for frequent reapplication due to the low stability and short half-life of the drugs. To

[a] *School of Electrical Engineering, Korea Advanced Institute of Science and Technology (KAIST), Daejeon, 34141, Republic of Korea. E-mail: kyungcc@kaist.ac.kr*
[b] *Center for Bio-Healthcare Materials, Bio-Convergence Materials R&D Division, Korea Institute of Ceramic Engineering and Technology, Cheongju, 28160, Republic of Korea. E-mail: dksung@kicet.re.kr*
[c] *Department of Chemical and Biomolecular Engineering, Yonsei University, Seoul, 03722, Republic of Korea*
[d] *Department of Pharmaceutics, College of Pharmacy, Chungbuk National University, Cheongju, 28644, Republic of Korea. E-mail: cpark@cbnu.ac.kr*
[e] *Department of Dermatology, Seoul National University Bundang Hospital (SNUBH), Seongnam, 13620, Republic of Korea*
[f] *Department of Information Display, Kyung Hee University, Seoul, 02447, Republic of Korea. E-mail: yongmin@khu.ac.kr*
† These authors contributed equally to this work.

overcome these hurdles, drug delivery systems (DDS) improve upon existing therapies by stably protecting the drugs and precisely controlling their release to maximize delivery efficiency.[5,6] Energy-based wearable devices offer a more advanced therapeutic paradigm, employing non-invasive energy to simultaneously enhance drug delivery efficiency and directly stimulate intrinsic cellular repair mechanisms.[7–12]

A DDS is an advanced technology that surpasses conventional, passive methods of drug administration.[13] By responding to the wound microenvironment, this system precisely releases drugs to enhance efficacy and reduce resistance. For example, stimuli-responsive carriers based on ferrocene nanoparticles (FNPs) can react to the elevated levels of ROS commonly observed in wound tissues.[14,15] These nanoparticles can be loaded with naturally derived compounds possessing antioxidant and regenerative properties, such as ascorbyl tetraisopalmitate (a vitamin C derivative) or alpha-tocopherol (vitamin E).[14,16] This design enables selective release in ROS-rich environments while enhancing the bioavailability of therapeutic agents, ultimately promoting effective wound repair. DDS have primarily been utilized in forms that respond to endogenous factors, such as ROS, at the wound site. However, the development of systems that respond to external stimuli is essential to achieve more precise and active control.[17] By controlling external energy, such as light, electromagnetic fields and ultrasound, with spatiotemporal precision to guide drug release, therapeutic effects can be maximized while side effects are minimized.[18] Furthermore, this extends beyond simple drug delivery, allowing the energy source itself to be utilized as a therapeutic agent.

Among these energy sources, phototherapy offers high selectivity and precision by using specific wavelengths of light to target molecules within cells and directly regulate their metabolism and function.[19] Phototherapy is a well-established approach to wound healing and can be broadly divided into two categories: photodynamic therapy (PDT) and photobiomodulation (PBM), differing fundamentally in their mechanisms and therapeutic goals.[20,21] PDT employs high-intensity light and a photosensitizer to generate large amounts of ROS, with the primary aim of killing bacteria or controlling infection at the wound site. In contrast, PBM uses low-intensity light without a photosensitizer to directly stimulate cellular metabolism, enhance mitochondria activation, and thereby promote tissue regeneration while reducing inflammation. PBM activates cells rather than destroying them, making it a safer and more appropriate modality for daily therapies such as wound healing, skin rejuvenation, and alopecia treatment. However, PBM monotherapy has an inherent limitation known as the 'biphasic dose–response,' where the therapeutic effect does not continuously increase with energy intensity but rather decreases after exceeding an optimal point.[22,23] This limitation makes a synergistic approach that combines PBM with drug therapy a promising alternative, moving beyond PBM monotherapy.

Indeed, several studies have demonstrated the additive therapeutic effects of combining PBM therapy with drug administration. For instance, laser-based PBM enhanced anti-fibrotic effects when combined with the naturally derived compound phloroglucinol, and showed a greater anti-inflammatory effect when used with nonsteroidal anti-inflammatory drugs (NSAIDs).[24,25] Similarly, LED-based PBM has been shown to accelerate the healing of atopic dermatitis and wounds when combined with drugs such as Tacrolimus or gelatin nanofibers.[26,27] The combination of PBM with specific drugs creates synergy for various therapeutic goals—such as reducing inflammation and promoting tissue regeneration.

Harnessing the full synergistic potential of PBM and DDS for practical therapeutic applications necessitates the development of a novel wearable platform capable of seamlessly integrating both modalities. Conventional approaches combining PBM with drug therapy have predominantly relied on lasers and LEDs, but these light sources are hampered by significant drawbacks. As point sources, they fail to deliver uniform illumination across the target area, pose a risk of localized thermal and light damage, and their rigidity and bulkiness preclude their integration into skin-conformable, wearable form-factors.[28,29] In response to these challenges, organic light-emitting diodes (OLEDs) are emerging as a promising next-generation light source. The intrinsic flexibility and surface light source of OLEDs permit their fabrication into diverse form factors—such as patches, textiles, and bands—that provide large-area, uniform emission.[30–33] Furthermore, the ability to precisely tune their emission wavelengths *via* microcavity structures allows for the selective delivery of only the therapeutically relevant light, optimizing treatment efficacy.[34,35]

Beyond the limitations of the light source, conventional approaches have largely been confined to a passive integration, wherein a PBM platform is merely superimposed onto a drug-loaded substrate like gelatin or S.ol.[27,30] This absence of active crosstalk forces each component to function in isolation, thereby precluding any possibility of true synergistic effects. While some studies have paired light-responsive DDS with LEDs, this approach often relegates light to the role of a simple trigger for drug release.[36,37] This paradigm is fundamentally distinct from a truly active therapeutic combination, which seeks to concurrently harness and amplify the therapeutic benefits of both the light itself (PBM) and the delivered drug.

Herein, we introduce a light-driven combination therapy that synergistically integrates PBM with a PBM-triggered DDS. Advancing beyond previous works that focused on either flexible PBM platforms or light-responsive DDS alone, our research centered on developing a wearable platform with electro-optical properties co-optimized for both modalities. The core of this platform is a wearable red OLED patch featuring a therapeutically-ideal emission wavelength (600–700 nm) with a narrow full width at half maximum (FWHM) of 38 nm. This device demonstrates excellent thermal stability (operating at 31 °C) and robust operational reliability (over 300 hours) at a PBM-relevant optical power density of 5 mW cm^{-2}. A key innovation is the utilization of the subtle levels of ROS generated during PBM as an endogenous trigger for drug release. We evaluated the optimal conditions for the ROS-responsive drug

release kinetics of CA@FNPs *in vitro*, and assessed therapeutic efficacy through both *in vitro* studies and *in vivo* experiments. The efficacy of this synergistic approach was validated through both *in vitro* studies with fibroblasts and *in vivo* experiments on a mouse skin wound model, which confirmed accelerated wound closure and significant histological improvements. Ultimately, this work establishes an effective strategy for combined wound therapy and pioneers the use of wearable OLEDs to integrate PBM with a ROS-responsive DDS that operates *via* an endogenously driven, biochemically self-regulating, negative-feedback-like mechanism within tissue, paving the way for next-generation wound management systems.

Results and discussion

System concept and operating principle: wearable platform for active photochemotherapy

Previous OLED-based phototherapy platforms for wound healing have been limited to either stand-alone PBM or simple passive integrations of PBM with drugs.[28,29,32–34,38–44] Specifically, stand-alone PBM is constrained by a biphasic dose–response, which imposes a therapeutic ceiling on its efficacy. On the other hand, passive integrations, where a light source is merely placed over a drug patch, suffer from uncontrolled release kinetics and lack the crucial crosstalk needed for a true synergistic effect.[27,30] To overcome these distinct yet interconnected limitations, we introduce a wearable OLED-based combination therapy that actively integrates a skin-conformable red OLED with a PBM-triggered DDS, thereby extending conventional PBM into an active photo-chemo therapy. The red light emitted by the OLED plays a dual role: it provides therapeutic PBM and, through PBM-associated ROS generation, serves as an endogenous stimulus to activate the ROS-responsive DDS. A conceptual illustration of this strategy is shown in Fig. 1a.

The platform's components were designed explicitly for this active therapeutic role. An OLED was selected for its ability to be fabricated on flexible polymer substrates, such as PET, PI, and parylene C.[31,45] It enables a thin, skin-conformable patch suitable for direct attachment to human and mouse skin (Fig. 1b, left). The OLED was optical-engineered to emit red light in the 600–700 nm range, an interval widely reported as optimal for stimulating mitochondrial activity and promoting wound repair, so as to maximize PBM efficacy.[28] To complement the optical module, we encapsulated the therapeutic agent CA within ROS-responsive FNPs, a process that

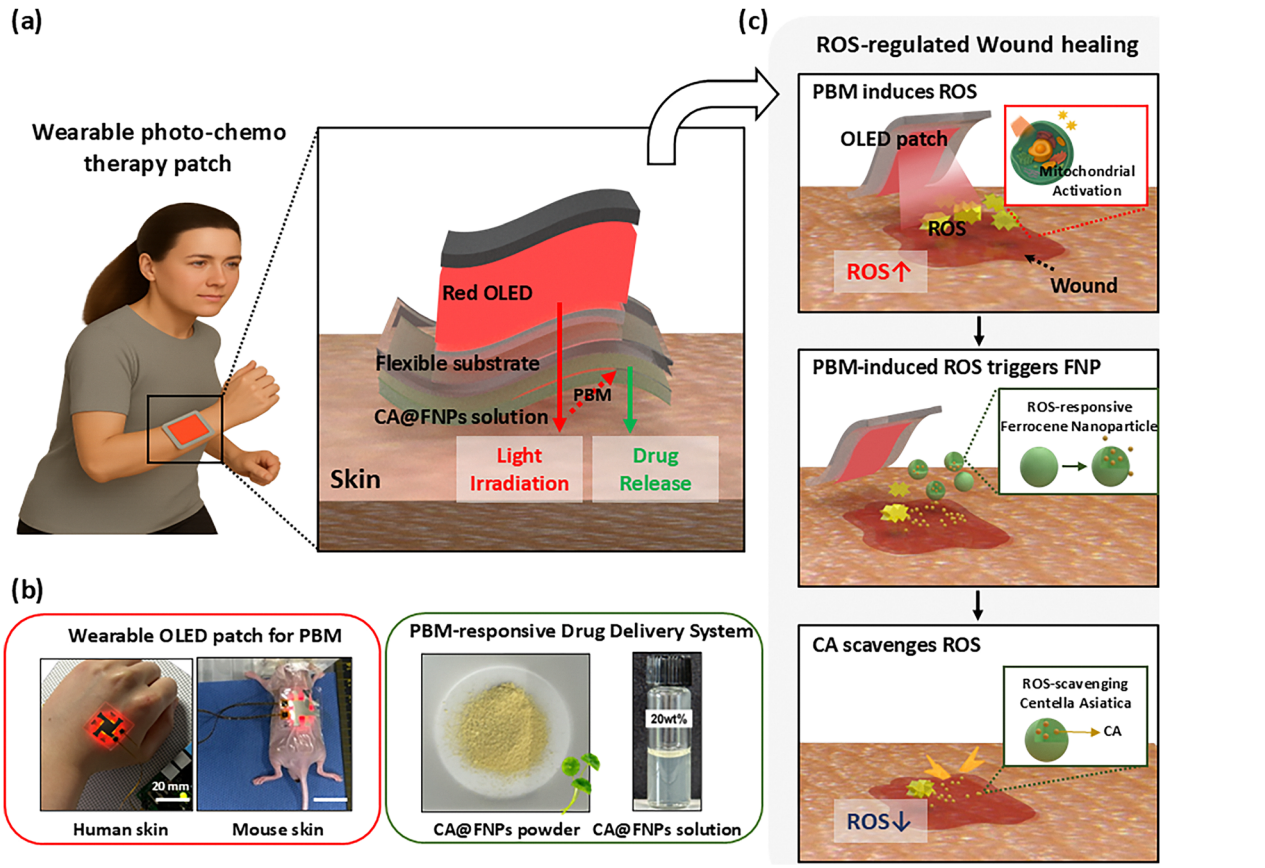

Fig. 1 Conceptual illustration of the wearable photo-chemotherapy patch for ROS-regulated wound healing. (a) Schematic illustration of the wearable photochemotherapy patch attached to a human. (b) Design and components of the wearable photo-chemotherapy patch. (c) Mechanism of ROS regulation for wound healing.

yielded CA@FNPs. These FNPs are engineered to selectively disintegrate in ROS-rich microenvironments, releasing their encapsulated agents on demand (Fig. 1b, right).[14,46]

The therapeutic mechanism is governed by a single, strategic redefinition of ROS:[47,48] from a purely detrimental byproduct in chronic wounds to a controlled, local trigger for drug release.[49–51] When red light from the OLED patch initiates PBM, it is associated with an increase in ROS that can activate the ROS-responsive FNPs to release CA as validated by *in vitro* release kinetics The released antioxidant CA then scavenges excessive ROS, helping restore redox balance and tissue homeostasis.[4,52] This light-enabled mechanism couples PBM with ROS-responsive on-demand drug release, thereby supporting an optimized wound microenvironment for accelerated healing (Fig. 1c, Fig. S1).

Fabrication and structure of the wearable photo-chemotherapy patch

Fig. 2a shows the schematic and structure of the wearable red OLED patch, which constitutes the core of the proposed wearable photo-chemo therapeutic patch. The device was fabricated on a flexible PET substrate (75 μm) and employed a microcavity structure with a semi-transparent Ag anode (30 nm) and a reflective Al cathode (100 nm) to adjust the emission wavelength.[28] A thin-film encapsulation, consisting of 1.5 dyads of AZ (Al_2O_3/ZnO) and a Si-based polymer, was applied to both the top and bottom of the OLED to prevent the penetration of moisture and oxygen, which are detrimental to organic electronic devices.[53] The detailed fabrication process is provided in the Methods section and SI (Fig. S2).

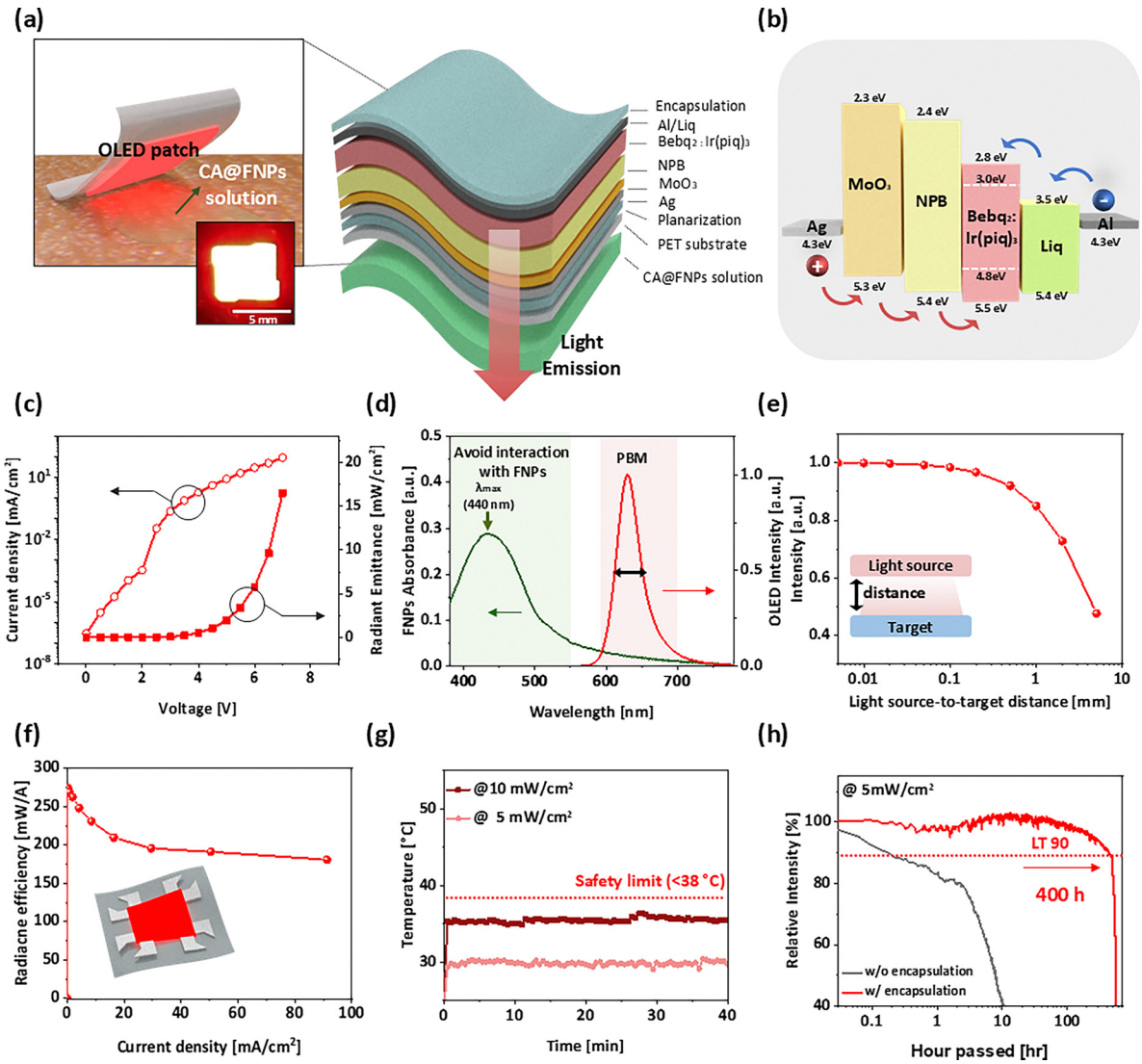

Fig. 2 Characterization of a physiochemical OLED patch integrated with PBM-responsive DDS. (a) Schematic illustration of the OLED patch and cross-sectional structure (inset photograph: emitting OLED in a dark environment). (b) The energy band diagram of the red OLED patch. (c) JVR. (d) EL spectrum of OLEDs and light absorption spectrum of FNPs. (d) Wavelength-engineered EL spectrum. (e) Intensity depending on light source to target distance. (f) Radiance efficiency. (g) Thermal stability through operating temperature. (h) Operating reliability through lifetime.

As illustrated in Fig. 2b, the red OLED patch was engineered with an optimal alignment of energy barriers at the layer interfaces to achieve good opto-electrical characteristics, and it emits red light due to the energy band gap of the emitting layer ($Bebq_2$:$Ir(piq)_3$).[22,29] The OLED patch exhibited stable electro-optical performance, achieving a radiant emittance exceeding 15 mW cm^{-2} at a driving voltage below 8 V (Fig. 2c). This output is more than threefold higher than the typical irradiance required for PBM therapy (5 mW cm^{-2}), confirming that the device provides sufficient optical power for therapeutic applications.

Because PBM relies on only low-level light, its therapeutic effect is highly dependent on wavelength, intensity, and energy dose.[49] In a combined PBM–drug delivery system, preventing parasitic optical interactions between the light and the drug carriers (CA@FNPs) is therefore critical. FNPs exhibit a maximum absorption wavelength at 440 nm due to their molecular structure consisting of an iron atom and two cyclopentadienyl rings. The majority of its absorption band is in the region below 600 nm.[54] When light in this range is applied, a portion of the optical energy is absorbed by FNPs before reaching the tissue of skin, reducing PBM efficiency and potentially inducing photodegradation of the FNPs. The OLED emission was engineered to avoid the FNP absorption band while remaining within the optimal PBM window (600–700 nm). To engineer the desired emission wavelength, the optimal thickness of the organic layer was determined through MATLAB simulations (Fig. S3). Based on these results, the OLED's microcavity was fabricated by adjusting the organic layers' thickness. This approach yielded a red OLED with a peak emission wavelength of 630 nm and a narrow full width at half maximum (FWHM) of 38 nm (Fig. 2d).

The skin-conformable OLED patch represents an ideal PBM light source because it can deliver optical energy to the target tissue with minimal loss. Optical simulations analysis using LightTools revealed that irradiance decreases sharply as the distance between the light source and the target surface increases (Fig. 2e, Fig. S4 and S5). It showed that light loss was below 1% when the gap was less than 0.1 mm, but rose to 7% at 1 mm and to 56% at 10 mm. These indicate OLED patches must be wearable, conformable, and fully adherent to the skin surface to eliminate light loss and ensure accurate therapy.

The wearable device also exhibited excellent radiance efficiency and thermal stability, both critical for practical wearable applications. The OLED patch achieved a maximum efficiency of 274 mW A^{-1} (Fig. 2f). This allowed the therapeutic irradiance of 5 mW cm^{-2} to be achieved at a low current density of only $\sim$18.2 mA cm^{-2}, directly minimizing power consumption and thermal load. Regarding thermal stability, the temperature of the OLED's surface saturated at 31 °C within one minute under 5 mW cm^{-2} irradiation, and at 36 °C even at a higher intensity of 10 mW cm^{-2} (Fig. 2g, Fig. S6). Both temperatures are below the threshold for low-temperature burns (38 °C), allowing for safe long-term contact with the skin.[55]

Long-term reliability was evaluated under continuous operation at 5 mW cm^{-2} (Fig. 2h). Unencapsulated devices exhibited rapid degradation, with luminance dropping below 50% of the initial value within 10 hours. In contrast, OLED patches with thin-film encapsulation maintained nearly their initial performance for over 400 hours, confirming outstanding operational stability. Based on the LT90 criterion, the encapsulated OLED patch exhibited an LT90 lifetime of $\sim$434 h at 5 mW cm^{-2}. Given that our *in vivo* PBM protocol operates the device for only 20 min per session, this corresponds to $\sim$1300 treatment sessions while maintaining 90% of its initial output.

In addition, to assess wearability-relevant robustness, the encapsulated OLED patches were subjected to repeated bending and water exposure tests. The devices showed negligible changes in electro-optical characteristics after cyclic bending at a radius of r = 10 mm, and maintained nearly identical performance after 1 h water dipping, confirming mechanical fatigue resistance and moisture tolerance (Fig. S7 and S8).

Characterization of PBM-triggered DDS

PBM-triggered CA@FNPs are the second core component of our therapeutic platform. Fig. 3a presents their composition and includes images of the prepared solutions, which had a more pronounced yellowish color with increasing loading contents of CA@FNPs. Even at the highest loading (40 wt%), the solution remained clear without visible precipitation. FNPs are ROS-responsive nanocarriers capable of effectively encapsulating hydrophobic drugs and selectively releasing them in ROS-rich environments such as wound sites.[56,57] To create these, we synthesized a polymer incorporating both hydrophilic PEGMA and MA, as well as hydrophobic FMMA monomers, resulting in an amphiphilic and ROS-responsive ferrocene-based polymer, poly(FMMA-*r*-PEGMA-*r*-MA), and confirmed its successful synthesis through NMR and GPC analysis (Table S1 and Fig. S9).[46] Upon exposure to ROS, the ferrocene moiety within the polymer backbone is oxidized to ferrocenium, shifting its characteristic from hydrophobic to hydrophilic. This redox transition induces structural instability in the nanoparticle, leading to swelling and eventual collapse, thereby releasing CA from CA@FNPs. This property is particularly advantageous for naturally derived drugs, which are typically hydrophobic and otherwise difficult to deliver.[46,58]

Transdermal drug delivery systems require meeting key criteria for their properties and stability. The drug particle size should remain below 300 nm for deep skin penetration, and a uniform polydispersity index (PDI) of less than 0.3 is required to regulate consistent drug release and efficacy, in accordance with FDA guidelines.[59] In addition, long-term storage stability and resistance to processes such as lyophilization are essential. To identify the optimal formulation that satisfies these requirements, we prepared CA@FNPs with different drug-loading contents (0, 10, 20, and 40 wt%), characteristics and stability, which were systematically evaluated using dynamic light scattering (DLS) analysis.

All formulations initially exhibited well-defined nanoparticles with diameters below 200 nm and PDI values under 0.2, confirming high uniformity (Fig. 3b and c). The drug loading content (LC) and efficiency (LE) were quantified using

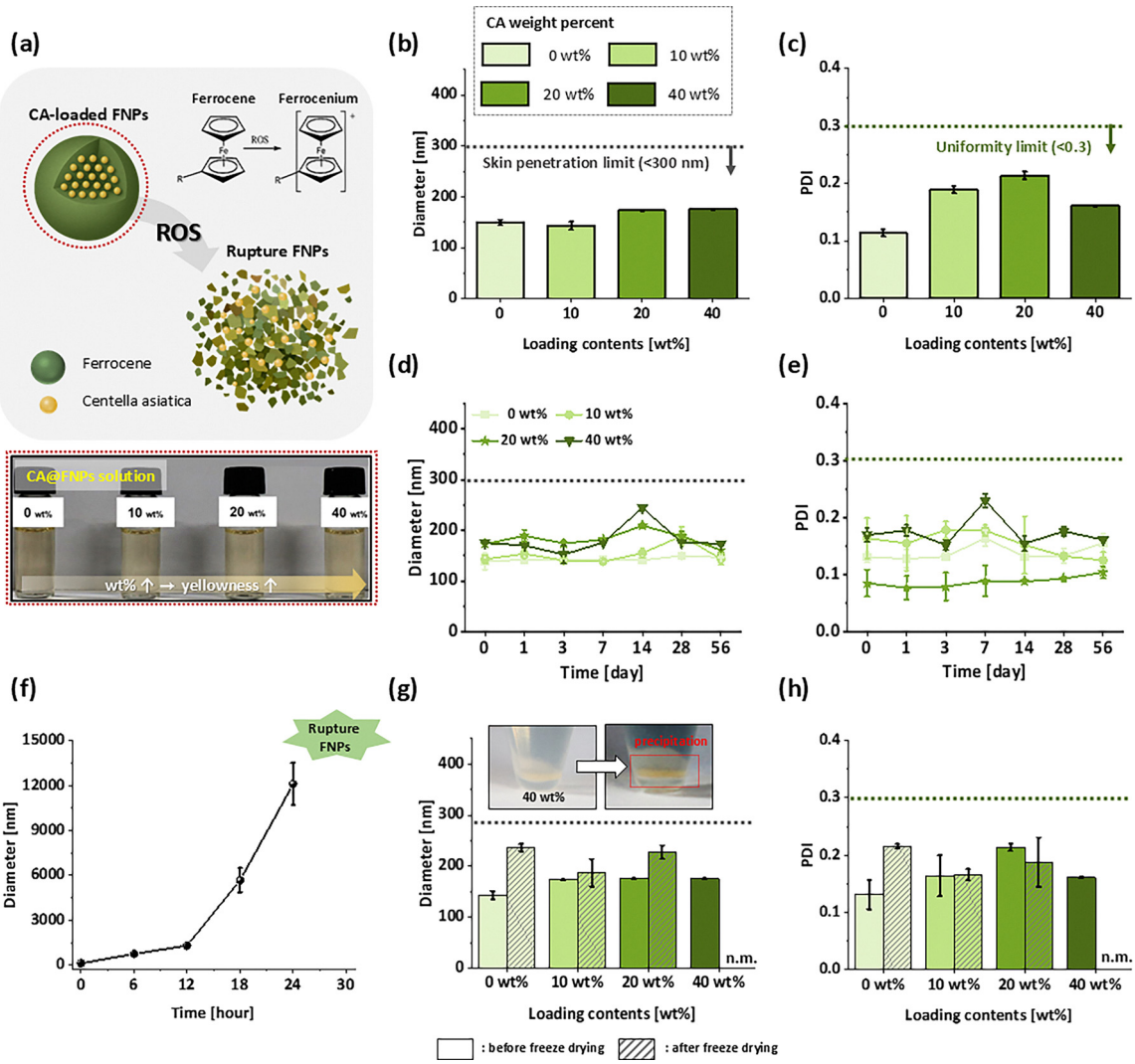

Fig. 3 Stability and properties of ROS-responsive CA@FNPs. (a) Schematic illustration and photograph of CA@FNPs. The initial properties of (b) hydrodynamic diameter, and (c) polydispersity index (PDI) depending on loading content. Reliability analysis over 8 weeks for (d) hydrodynamic diameters and (e) PDI. (f) 20 wt% CA@FNP diameter changes after being in a ROS-rich environment. Re-dispersion stability of CA@FNP (g) hydrodynamic diameter and (h) PDI before and after freeze drying (inset photograph: before and after re-dispersion of CA@FNPs 40 wt; n.m.: not measurable).

high-performance liquid chromatography (HPLC). Specifically, the 10, 20, and 40 wt% formulations achieved LC values of 9.5%, 18.55%, and 36.66%, and LE values of 95.05%, 92.77%, and 91.65%, respectively.

When the formulations became unstable, the hydrodynamic diameter increased by nearly an order of magnitude and the PDI exceeded 0.3. Long-term stability tests further showed that all formulations maintained colloidal stability for 8 weeks, with no significant changes in diameter or PDI (Fig. 3d and e). These results indicate that the prepared CA@FNPs maintain the essential physical characteristics required for effective and stable transdermal drug delivery.[16]

Freeze-drying enhances drug stability by removing water while preserving active structures, preventing degradation of heat-sensitive substances, and ensuring long-term storage. The resulting product is easy to transport and can be readily reconstituted before use. However, differences emerged during lyophilization, a process relevant to practical product manufacturing. When redispersed after freeze-drying without cryoprotectants such as trehalose or glucose, formulations at 20 wt% or lower maintained their size distributions. By contrast, the 40 wt% formulation exhibited aggregation and precipitation (Fig. 3g, inset), precluding measurement of the hydrodynamic diameter and PDI. These findings established 20 wt% as the optimal loading concentration, balancing high drug content with efficiency and stability.

Finally, the functionality of the optimized 20 wt% CA@FNPs was validated under ROS-rich conditions. An artificial ROS-rich environment (100 μM H_2O_2) was applied, and the particle size was monitored over time. The diameter, initially below 200 nm, expanded beyond 20 000 nm after 48 hours, indicating complete structural disintegration. This collapse confirms successful oxidation of the ferrocene core and verifies that the nanoparticles can reliably release CA from CA@FNPs in

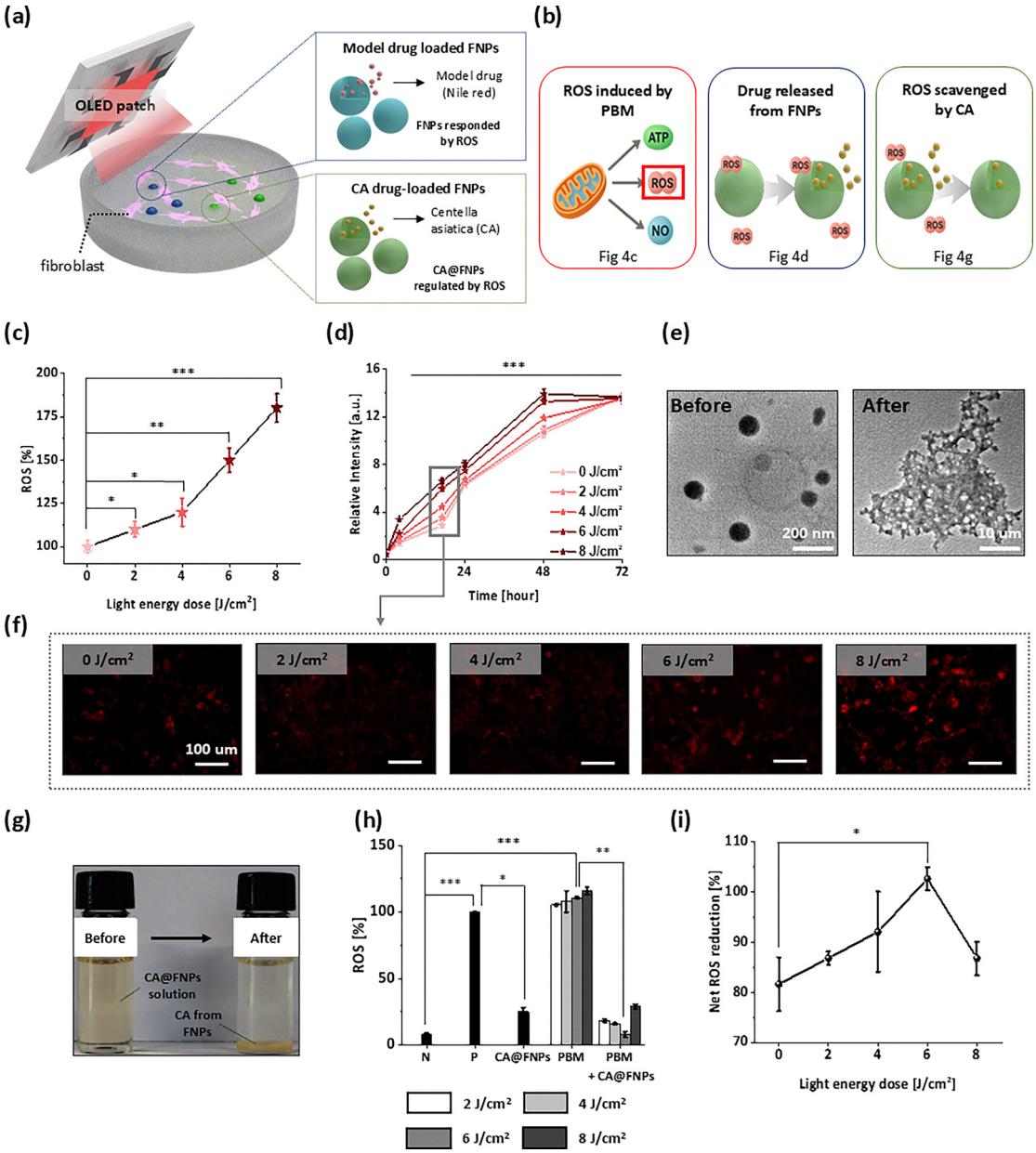

Fig. 4 Cooperative interaction between ROS-initiative PBM and ROS-responsive CA@FNPs. Schematic illustration of (a) PBM-triggered FNPs experiments and (b) cooperative mechanism of PBM and CA@FNPs. (c) Quantification of intracellular ROS levels in NIH-3T3 fibroblasts induced by different PBM doses under basal conditions. (d) Release profile of Nile Red from FNPs in PBS (pH 7.4) at 37 °C as a function of PBM dose. (e) TEM image of FNPs showing ROS-responsive structural changes. (f) Fluorescence microscopy images showing Nile Red release from FNPs after 12 hours. (g) Photograph of a CA@FNP solution before and after exposure to ROS. (h) *In vitro* ROS regulation by CA@FNPs and/or PBM in NIH-3T3 fibroblasts under high-ROS conditions, measured using an H_2DCFDA assay (N: negative control, untreated; P: positive control, H_2O_2 treated). (i) Net ROS reduction achieved by the combination of CA@FNPs and varying PBM energy doses. (Data are presented as mean ± SD (n = 3). *$p < 0.05$, **$p < 0.01$, ***$p < 0.005$ relative to the control group.)

response to ROS. The optimized 20 wt% CA@FNPs function as a robust, stimulus-responsive drug delivery system suitable for ROS-related combination therapy.

To verify the cooperative interaction between PBM induced by the OLED patch and CA@FNPs, we performed *in vitro* experiments using two types of FNPs: one loaded with a model drug (Nile Red) and the other with the CA drug (Fig. 4a). Nile Red-loaded FNPs were used to test whether PBM-induced ROS could trigger nanoparticle activation, and CA-loaded FNPs were employed to evaluate the ROS-regulating effect of PBM and CA@FNPs.

In Fig. 4b, the combination therapy of PBM and CA@FNPs involves a stepwise interaction. First, red light from the OLED irradiates the cells, eliciting the intrinsic therapeutic benefits of PBM while generating byproducts such as ROS, ATP, and NO.[19,49] Among these, ROS interacts with FNPs, inducing

structural collapse and releasing the encapsulated CA. Finally, the released CA scavenges the ROS, restoring the cellular microenvironment to a normal state.

ROS plays a dual role in wound healing: excessive accumulation delays repair, whereas a transient increase by PBM can serve as a signaling cue to initiate drug release.[60] To explore this dynamic, we investigated the ROS levels in NIH-3T3 fibroblasts, a representative skin cell line, using the H_2DCFDA assay. We first analyzed the dose–response relationship between PBM irradiation and ROS generation under basal conditions. As shown in Fig. 4c, intracellular ROS levels in fibroblasts increased in a dose-dependent manner with the applied light energy dose. Compared to the control group, ROS generation increased by 10%, 20%, 50%, and 80% following irradiation at 2, 4, 6, and 8 J cm^{-2}, respectively.

To confirm that PBM-induced ROS facilitates nanoparticle release, we quantitatively monitored the release of the fluorescent model drug Nile Red from FNPs over 72 hours. As a fluorescent probe, Nile Red release was quantified by changes in fluorescence intensity. As shown in Fig. 4d, light irradiation significantly accelerated drug release in a dose-dependent manner, with the release rate reaching up to 2.3-fold higher than that of the control group at 17 hours. This accelerated release was also visually confirmed by fluorescence microscopy (Fig. 4f). The release rate differences persisted for up to 48 hours, after which nearly all groups converged to similar release levels by 72 hours. These results confirm that FNPs effectively release their loaded drugs in response to ROS, a mechanism attributable to nanoparticle swelling and structural collapse under a ROS-rich environment, as depicted in Fig. 4e and Fig. S10.

The ROS responsiveness of CA@FNPs was also visually evident, with precipitation observed 48 hours after exposure to the ROS-rich environment (Fig. 4g). To further validate the cooperative ROS-regulating effect of PBM and CA@FNPs, we assessed ROS level changes in an oxidative environment established to mimic wound conditions. Our results first confirmed that PBM generates ROS from a normal baseline (Fig. 4c). Based on this finding, we evaluated the cooperative ROS-regulating effect in a high-stress environment designed to mimic wound conditions. For reference, the ROS levels for the negative control (representing a healthy state) and the positive control (high-ROS condition) were established at 8% and 100%, respectively. Treatment with CA@FNPs alone reduced ROS to 25%, whereas PBM alone at 2, 4, 6, and 8 J cm^{-2} increased ROS to 105%, 108%, 111%, and 116%, respectively. When PBM was combined with CA@FNPs, the elevated ROS levels were modulated to 18%, 16%, 8%, and 29%, respectively. Notably, the 6 J cm^{-2} combination dose was the most effective, reducing the ROS level to 8%—a level identical to the negative control and indicating a restoration to a near-healthy state.

To quantify the synergistic ROS scavenging effect, we calculated the net ROS reduction relative to the control baseline. As shown in Fig. 4i, this reduction was 82%, 87%, 92%, 103%, and 87% for light energy doses of 0, 2, 4, 6, and 8 J cm^{-2}, respectively. This indicates that 6 J cm^{-2} represents the therapeutic window—an optimal balance where sufficient ROS is induced to trigger CA release without exceeding the antioxidant capacity of CA@FNPs.

The ROS-regulating capability of the OLED-based PBM and CA@FNP system exhibits a biphasic tendency. Within the therapeutic window of 2–6 J cm^{-2}, PBM-induced ROS act as a signal to promote CA release from FNPs, and the released CA subsequently scavenges the ROS, forming a virtuous cycle that maximizes therapeutic efficacy. However, excessive energy (8 J cm^{-2}) produces ROS levels that surpass the antioxidant capacity of CA@FNPs, diminishing the overall therapeutic effect. This platform does not merely combine light and drug; rather, it actively modulates the wound microenvironment by leveraging PBM-induced ROS both as a trigger for drug release and as a target for the released drug to neutralize.

Optimization of OLED-based photochemotherapy in wound healing models

To verify cellular-level activity of the aforementioned ROS-regulating combination therapy, we sequentially evaluated its cytocompatibility and therapeutic efficacy in NIH-3T3 fibroblasts. Four experimental groups were established: Control, CA@FNPs alone, PBM alone, and PBM + CA@FNPs combination therapy (Fig. 5a). Safety was evaluated using the MTT assay, which reflects cell viability through metabolic activity, whereas therapeutic efficacy was assessed by the scratch assay, which tracks gap closure in a confluent monolayer as a measure of cell migration and proliferation (Fig. 5b).

To identify the optimal PBM conditions, experiments were designed based on the total light energy (J cm^{-2}) delivered to the cells. CA@FNPs were applied at 0.1 μg mL^{-1}, using the optimized 20 wt% formulation established previously (Fig. S11). PBM was performed with an OLED light source (5 mW cm^{-2}), with irradiation times adjusted to deliver 2, 4, 6, or 8 J cm^{-2} to cell culture. A custom-made jig was employed to maintain a constant distance (15 mm) between the OLED surface and the cells, ensuring consistent conditions and completed thermal isolation.

Cytotoxicity was assessed 24 hours post-treatment using an MTT assay (Fig. 5d). According to ISO 10993-5 standards, cell viability above 70% indicates biocompatibility. In all treatment groups—PBM alone, CA@FNPs alone, and the combination therapy—cell viability remained above this threshold, confirming the absence of cytotoxic effects.

Therapeutic efficacy was evaluated by the scratch assay over 72 hours (Fig. 5c). The combination therapy markedly accelerated wound closure, achieving a 30.82% recovery rate after 72 hours, compared with 16.53% for CA@FNPs alone and 16.09% for PBM alone (Fig. 5e). The enhanced effect was evident from the early phase: at 24 hours, wound closure reached 18.76% in the combination group, compared with 2.23% in the control, 8.74% with CA@FNPs, and 9.86% with PBM (6 J cm^{-2}) (Fig. S12 and Table S2). The trend for cell migration was biphasic, showing enhancement between 2 and 6 J cm^{-2} but a reduction at 8 J cm^{-2}, following a similar pattern to the cooperative interaction between PBM and CA@FNPs.

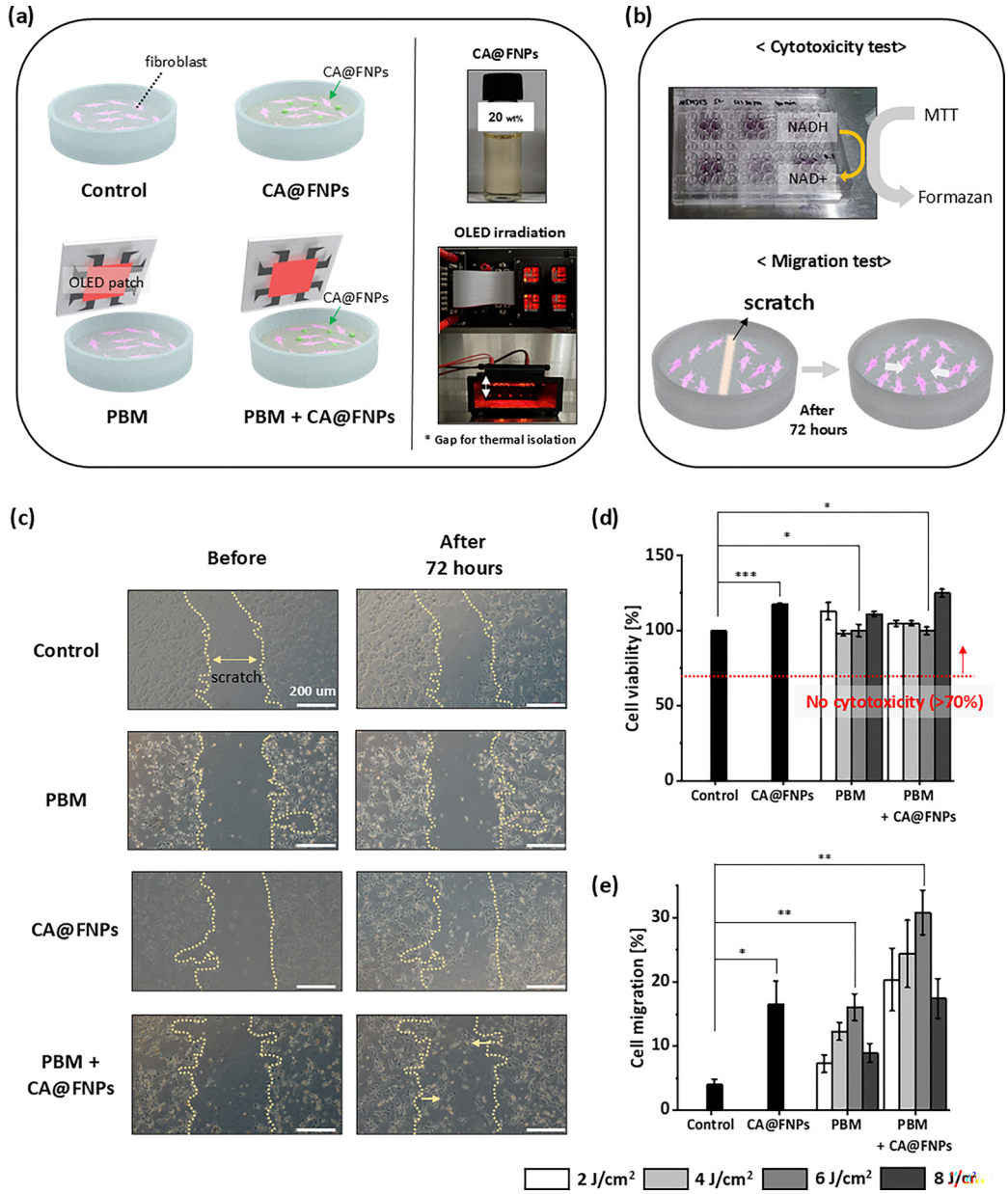

Fig. 5 *In vitro* testing using an MTT assay and scratch assay in NIH 3T3 fibroblast cells for ROS-regulatory wound healing effects. (a) *In vitro* experimental design and photographs of OLED operation and CA@FNP solution. (b) Schematic of the *in vitro* cytotoxicity and cell migration assays. (c) Photograph of the cell migration before and after 72 hours. (d) Result of cytotoxicity testing (24 hours) by OLED irradiation and CA@FNPs. (e) Result of migration testing (72 hours) by OLED irradiation and CA@FNPs. (Data are presented as mean ± SD (n = 3). *$p < 0.05$, **$p < 0.01$, ***$p < 0.005$ relative to the control group.)

The *in vitro* results in Fig. 5 demonstrate that the combination therapy is biocompatible (non-cytotoxic) and highly effective in promoting wound healing. Notably, the migration rate in the combination group (30.82%) was approximately equivalent to the additive effects of the individual groups (CA@FNPs 16.53% + PBM 16.09%), highlighting a complementary additive effect. These findings provide strong evidence for enhanced therapeutic efficacy *via* PBM-induced drug release: (1) PBM directly stimulates cell migration through OLED irradiation, and (2) concurrently, drug release from CA@FNPs improves the cellular environment. Importantly, the identification of 6 J cm^{-2} as the optimal energy dose in both Fig. 4 and 5 provides decisive evidence that this synergistic mechanism is indeed active at the cellular level.

The light energy dose for the animal study was set to 6 J cm^{-2}, a condition previously validated as optimal, consistently yielding the most effective therapeutic outcomes in both *in vitro* cell experiments (Fig. 5) and previous studies. Based on pre-validated experiments, we evaluated whether PBM combined with CA@FNPs improves wound healing *in vivo*.

As illustrated in Fig. 6a, CA@FNPs were applied to the wound area, followed by the attachment of a skin-conformable OLED

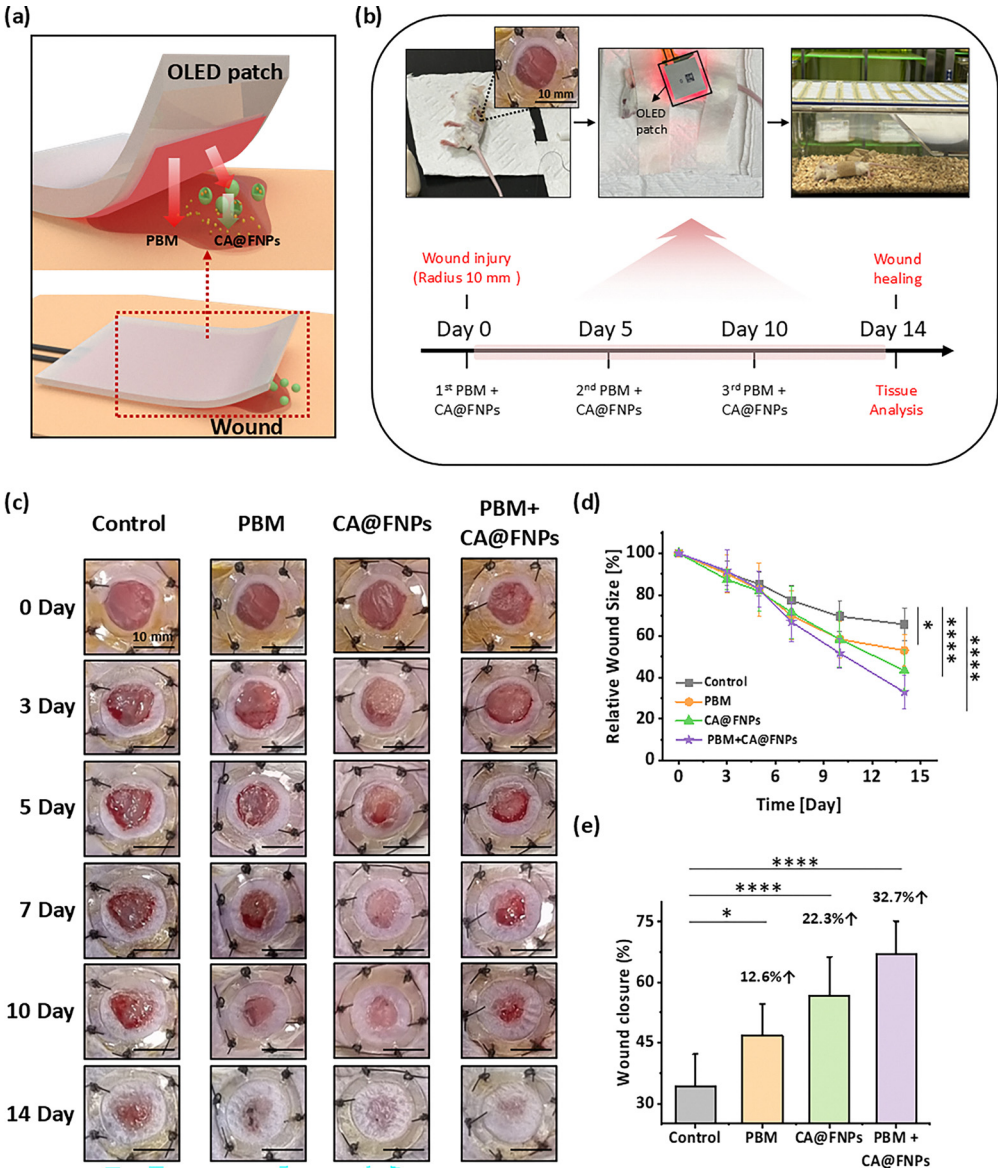

Fig. 6 *In vivo* wound healing efficacy for ROS-regulatory wound healing effects. (a) Schematic illustration of the wearable photo-chemotherapy patch. (b) Timeline of the *in vivo* wound healing test. (c) Representative images of mouse's wound site treated with the Control, OLED, CA@FNPs, and the combined OLED + CA@FNPs therapy. (d) Quantitative analysis of wound area reduction in each treatment group over 14 days. (e) Wound closure rates at day 14. (Data are presented as mean ± SD (n = 8). *$p < 0.05$, **$p < 0.01$, ***$p \leq 0.005$, ****$p \leq 0.001$ relative to the control group.)

patch to ensure efficient, loss-free delivery of light energy to the wound site. According to the schedule in Fig. 6b, a 10 mm full-thickness excisional wound was created on the dorsal skin of each mouse on Day 0. A silicone splint was fixed around the wound margin, thereby preventing the common phenomenon of wound contraction in rodents and promoting a re-epithelialization process more comparable to human physiology. While treatments were administered three times (Day 0, 5, and 10), wound closure was monitored over 14 days, after which tissue samples were collected for histological analysis.[61]

The therapeutic efficacy of PBM and CA@FNPs was then evaluated *in vivo*. Representative wound images and quantitative closure rates are shown in Fig. 6c. Wound size was normalized to 100% at Day 0 and tracked for 14 days. From Day 7 onward, the combination therapy group exhibited significantly faster healing than all other groups. On Day 14, the remaining wound area was 65% in the control, 53% in PBM alone, 43% in CA@FNPs alone, and 33% in the combination group (Fig. 6d). These values correspond to closure rates of 35%, 47%, 57%, and 67%, respectively (Fig. 6e). Thus, compared to the control, PBM, CA@FNPs, the combined treatment improved recovery by 12.6%, 22.3%, and 32.7%. These results confirm that PBM and CA@FNPs act with a strong additive effect *in vivo*, accelerating wound healing through a powerful complementary interaction that promotes skin regeneration.

To elucidate how the enhanced wound healing effects observed in Fig. 6 translated into tissue-level improvements, we performed a detailed analysis of wound samples harvested

on Day 14. As the healing process transitions to the maturation phase, the epidermis thickens and the vascular network is pruned back. Our analysis focused on two key markers: the maturation of the healing process *via* (i) epidermal barrier reconstruction and (ii) vascular stabilization (Fig. 7a).[62,63]

First, histological evaluation with H&E staining confirmed that the combination therapy group developed the thickest and most organized epidermal layer at 83 μm. This was significantly greater than the PBM-only (58.3 μm) and CA@FNP-only (59.5 μm) groups, and nearly twice that of the control group

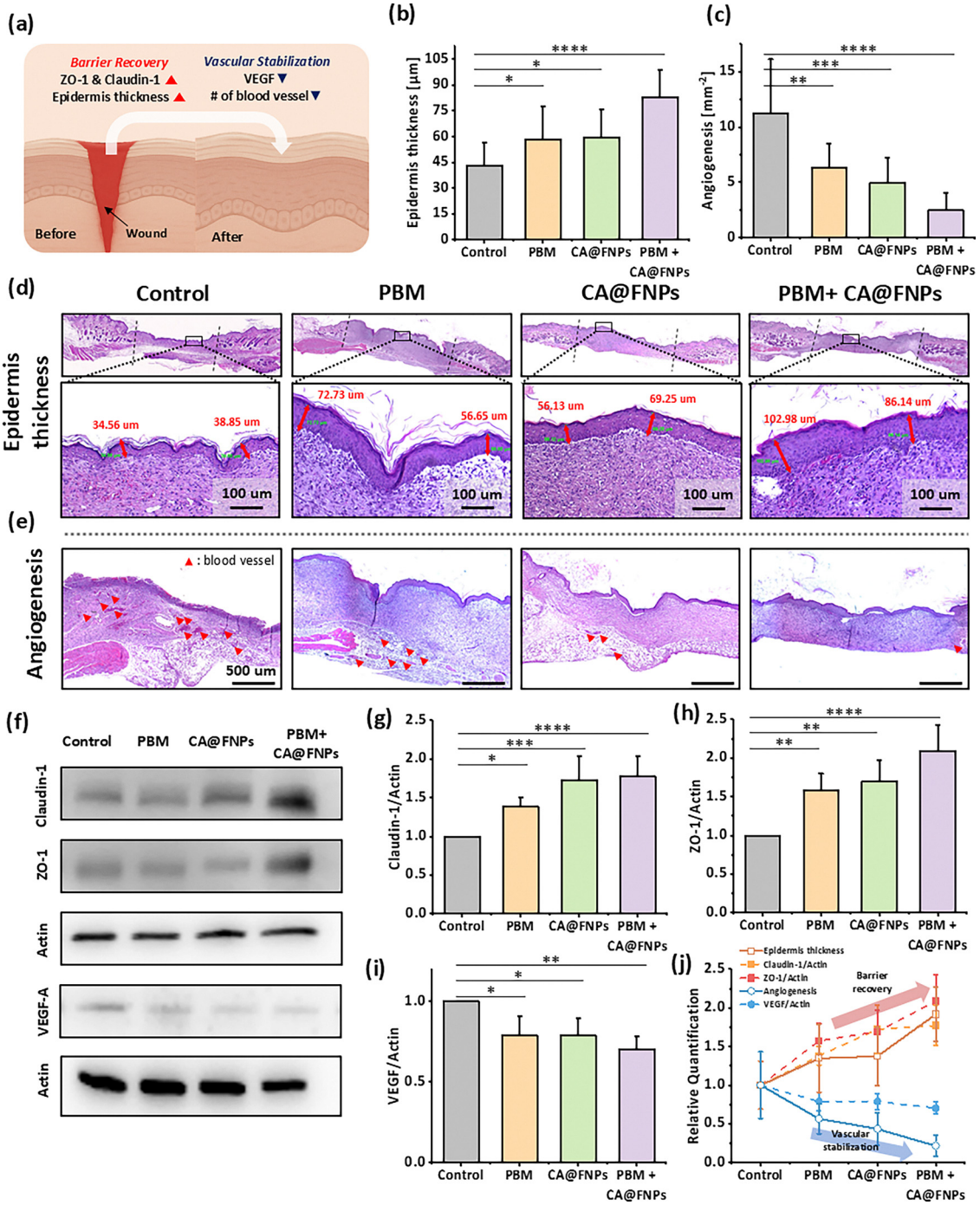

Fig. 7 Histological and western blot analysis of wound tissue on day 14 following treatment for ROS-regulatory wound healing effects. (a) Schematic illustration of histological changes during the wound healing process. Quantification of (b) epidermal thickness and (c) number of blood vessels (angiogenesis). Representative H&E-stained images of treated wound sections to evaluate (d) epidermal thickness and (e) angiogenesis. (f) Representative western blot images showing the expression of epidermal barrier and vascular-related factors in wound tissues. Quantitative analysis of (g) claudin-1 and (h) ZO-1 protein, and (i) VEGF-A expression levels based on densitometric measurements. (j) Histological tendency analysis. (Data are presented as mean ± SD. *$p < 0.05$, **$p < 0.01$, ***$p \leq 0.005$, ****$p \leq 0.001$ relative to the control group.)

Table 1 Comparative analysis of flexible photobiomodulation

Ref.	Form factor	Target	Light source	Combinational treatment	Light triggered	Light intensity [mW cm^{-2}]	*In vitro*	*In vivo*
This work	**Patch**	**Wound healing**	**OLED**	**Stimulus drug delivery system (CA@FNPs)**	○	**5**	○	○
28	Patch	Wound healing	OLED	✗	✗	5	○	✗
34	Patch	Wound healing	OLED	✗	✗	5	○	✗
38	Patch	Wound healing	OLED	✗	✗	5	○	✗
39	Patch	Wound healing	OLED	✗	✗	5	○	✗
32	Patch	Wound healing	OLED	✗	✗	5	○	✗
42	Patch	Wound healing	OLED	✗	✗	5	○	○
33	Patch	Wound healing	OLED	✗	✗	5	○	○
40	Patch	Hair loss	OLED	✗	✗	3	○	✗
44	Patch	Atopic dermatitis	OLED	✗	✗	5	✗	○
41	Catheter	Diabetes mellitus	OLED	✗	✗	0.58	○	○
29	Textile	Neonatal jaundice	OLED	✗	✗	2.58	○	✗
43	Probe	Optogenetic	OLED	✗	✗	100	✗	○
30	Patch	Antibacterial treatment	OLED	Extract solution (Sanguisorba officinalis L.)	✗	17	○	✗
27	Patch	Wound healing	LED	Gelatin nanofiber (HA–cross-linked gelatin nanofibrous gel)	✗	5–8	○	○

(43.2 μm) (Fig. 7b and d). This structural enhancement was further supported by molecular analysis, which showed the highest expression of the tight junction proteins claudin-1 and ZO-1.[64] Normalizing the target protein's expression to that of actin in each sample minimizes loading errors and enables the relative analysis of actual changes in the protein's expression. Relative to the control (normalized to 1), claudin-1 and ZO-1 expression reached 1.77 and 2.09 in the combination group, respectively, surpassing all other groups (Fig. 7g and h). These findings indicate that the therapy accelerates the formation of a quantitatively and qualitatively superior skin barrier.

Next, we assessed vascular stabilization, a hallmark of the transition to the late remodeling phase.[65] Histological analysis revealed the most significant reduction in blood vessel density in the combination therapy group, with a vessel area of only 2.5 mm^{-2}. This was a sharp decline compared to the CA@FNP-only (4.9 mm^{-2}), PBM-only (6.4 mm^{-2}), and control (11.3 mm^{-2}) groups (Fig. 7c and e). This observation was consistent with molecular data, where the expression of the pro-angiogenic factor VEGF-A in the combination therapy group dropped to 0.7 relative to the control group (Fig. 7i). Collectively, these results demonstrate that the combination therapy effectively promotes the transition from a highly vascularized, proliferative tissue to a stable, maturely remodeled state, finalizing the healing process. As indicated in Fig. 7j, the strong correlation between histological findings and key protein expression demonstrates the efficacy of the proposed combination therapy, which improves the complex wound environment through the dual action of strengthening the skin barrier and promoting vascular stabilization.

Conclusions

This study presents a skin-conformable combination therapy patch that seamlessly integrates OLED-based PBM with a PBM-triggered DDS to accelerate wound healing. This integrated approach represents a significant advancement over previous research, which has largely focused on PBM as a monotherapy or was limited to simply combining it with drugs, as detailed in Table 1. The core of our work is the demonstration of a synergistic therapy where the red OLED performs two critical roles simultaneously. First, it acts as a therapeutic light source that penetrates deep into the skin to induce a PBM effect without optical-interfering with the nanoparticles. Second, it functions as an active trigger, utilizing the ROS generated during the PBM process as a signal to induce drug release from CA@FNPs. Notably, this mechanism is an endogenously driven, biochemically self-regulating, negative-feedback-like process in which PBM-induced ROS triggers CA release and the released CA subsequently scavenges ROS.

Through comprehensive validation in an *in vivo* model, assessing both quantitative recovery (Fig. 6) and qualitative improvement (Fig. 7), we have definitively demonstrated that the proposed combination therapy of OLED–PBM and CA@FNPs enables enhanced wound healing. This success is attributed to a mechanism in which PBM-induced ROS acts as a signal to trigger the release of the CA drug, which in turn scavenges the ROS to establish an optimal therapeutic environment. This process was shown to be a superior treatment modality that rapidly and robustly reconstructs the skin barrier and swiftly transitions the wound to a mature, stable phase.

In conclusion, this work provides a new pathway for photochemo combination therapy using flexible OLEDs, synergistically integrating treatments with distinct mechanisms. Although the focus of this research is skin wound healing, the demonstrated principle of active drug control using light holds broad potential as a platform technology to maximize the efficacy of future PBM-based therapies. Future work could focus on adapting this platform to treat a broader range of diseases, including chronic wound models, by targeting their specific pathological features.

Methodology

OLED patch fabrication

A flexible OLED patch was fabricated onto a PET (75 μm) substrate. Atomic layer deposition (ALD) and spin coater were employed to deposit barriers for planarization and passivation

of the OLED patch.[28,53] A total of 1.5 dyads of nanolaminate layer (Al_2O_3 and ZnO) and SiO_2 polymer were fabricated. The OLED was fabricated in the following order: first, MoO_3 (5 nm) was deposited as a hole injection layer (HIL) on Ag 30 nm, as an anode. Subsequently, after NPB (62 nm) as a hole transport layer (HTL) was deposited, $Bebq_2$:$Ir(piq)_3$ (host:dopant) (70 nm, 8 wt%) as an emission layer (EML) was deposited. Finally, Liq (1 nm) was deposited as an electron injection layer (EIL), and aluminum (Al, 100 nm) as the cathode. The OLED was passivated with a 1.5 dyads nanolaminate oxide/polymer structure, as in the previous process.

Fabrication of CA@FNPs

We used a ferrocene based on polymer (poly(FMMA-*r*-PEGMA-*r*-MA)) previously synthesized through optimized radical polymerization to make FNP. A nanoprecipitation method was used to prepare the CA@FNPs. First, THF was dissolved in powdered CA (0, 0.5, 1, 2) mg at 950 μl and added to the optimized polymer solution (10%) 50 μl so that the CA concentration in the polymer had a drug concentration of 0%, 10%, 20%, and 40%, respectively. After stabilizing the mixture for 2 hours, each polymer solution containing CA was slowly precipitated in 5 mL of deionized water (DIW) by nanoprecipitation while stirring at 530 rpm using a 30G syringe. Afterwards, the potentially harmful THF solvent was removed by natural volatilization in a hood for 24 hours. Hydrodynamic measurements were performed using DLS.[15,66]

ROS responsive properties of CA@FNPs

To investigate the ROS reactivity of the optimized 20% CA@FNPs, CA@FNPs were treated with 100 μM H_2O_2 as an oxidizing agent. Nanoparticles were monitored using DLS for changes in particle size at various time points (0, 6, 12, 18, 24, and 48 h). Additionally, 48 hours later, the morphological changes and appearance of the oxidized CA@FNPs were observed using TEM.[67,68]

In Vitro cell-based experiments

Cell culture. NIH-3T3 fibroblast cells were cultured in Dulbecco's adapted Eagle's medium (DMEM, Gibco, Frand Island, NY, USA) complemented with 10% fetal bovine serum (FBS, Gibco, Frand Island, NY, USA), and 1% penicillin–streptomycin (PS, Gibco, by Gibco, Frand Island, NY, USA) at 37 °C, 5% CO_2 conditions.

Determination of the intracellular OLED-initiative ROS. An H_2DCFDA assay was used to determine the intracellular OLED-initiated ROS. NIH-3T3 cells were seeded in 96-well plates with a concentration of 10 000 cells per well and cultured at 37 °C, 5% CO_2 for 24 hours. After incubation, 200 μl of PBS were added to each well, and the OLED was delivered for energy doses from 2 to 8 J cm^{-2}. Additionally, a control group that was not irradiated by OLED was used as a control group. After aspirating PBS, each well was treated with 200 μL of DMEM (containing 10% FBS and 1% PS), followed by a 4 hour incubation. After incubation, the NIH-3T3 cells were exposed to a 10 μM H_2DCFDA solution, which served as a fluorescence indicator for ROS, and were incubated in the dark for 90 minutes. ROS generation of the NIH-3T3 cells was assessed by estimating dichlorofluorescein (DCF), which was oxidized by ROS, and by the fluorescence intensity at an emission wavelength of 535 nm (excitation wavelength: 485 nm) using a microplate reader.[69,70]

Drug release rate to test OLED-initiated ROS responsivity. To assess the drug released from the FNPs in an OLED irradiated environment, we loaded the fluorescent substance Nile Red as a model drug into the FNPs. Subsequently, we evaluated the release of Nile Red using fluorescence microscopy. NIH-3T3 cells were cultured in 6-well plates at a density of 100 000 cells per well and cultured at 37 °C for 24 hours. Afterwards, 1 ml of PBS was added to each well, and the OLED was delivered for energy dose from 2 to 8 J cm^{-2}. Additionally, a control group that was not irradiated by OLED was used as a control group. After that, suspensions of Nile Red-loaded FNPs were added to each well, and the fluorescence of Nile Red (with an emission wavelength of 628 nm and excitation wavelength of 549 nm), indicating the release rate of Nile Red from FNPs, was measured over time using a fluorescence microscope (DMi8 microscope; Leica, Germany) at different time points (0 to 72 hours).[71,72]

Determination of intracellular ROS regulation. An H_2DCFDA assay was used to determine the intracellular ROS regulation in OLED irradiation and CA@FNPs. NIH-3T3 cells were incubated in 96-well plates at a density of 10 000 cells per well and cultured at 37 °C, 5% CO_2 for 24 hours. After incubation, ROS was generated in NIH-3T3 cells by OLED irradiation for energy doses ranging from 2 to 8 J cm^{-2} and 50 μM H_2O_2 as an oxidative stress agent. After applying a specific treatment to the samples, changes in the levels of ROS were assessed using the following procedure. First, suspensions of CA@FNPs 20 wt% with 0.1 μg mL^{-1} concentration were applied to ROS induced cells. For comparison, a negative control group without H_2O_2 and a positive control group with H_2O_2 were used. Then, NIH-3T3 cells were added with a 10 μM H_2DCFDA solution, a fluorescent indicator for ROS, and incubated in darkness for 90 minutes. Subsequently, ROS levels in the NIH-3T3 cells were evaluated by measuring the fluorescence intensity of DCF, oxidized by ROS, at 535 nm emission (excitation: 485 nm) using a microplate reader from BioTek in Winooski, VT, USA.[69]

In vitro wound healing assay

Cytotoxicity test. An MTT assay was used to test cytotoxicity after treatment with OLED irradiation and CA@FNPs. NIH-3T3 cells were seeded in 96-well plates at a density of 10 000 cells per well and cultured at 37 °C for 24 hours. Afterwards, they were treated with CA@FNPs, OLED irradiated, and CA@FNPs plus OLED for durations ranging from 0 to 40 minutes and seeded for 24 h. Following that, a 1 mg mL^{-1} MTT solution was introduced into the culture medium. Subsequently, DMEM solution (containing 1% penicillin–streptomycin and 10% FBS) was applied to each well in the plate, and the cells were incubated for 3 hours. In the final step, the medium was washed with PBS, and purple formazan dye crystals were

dissolved using DMSO-d_6. The absorbance of the formazan generated by viable cells was then quantified at a wavelength of 570 nm using a microplate reader.[73,74]

Migration test. A scratch assay was used to test the wound healing properties of OLED irradiation and CA@FNPs. NIH-3T3 cells were cultured in 24-well plates at a density of 200 000 cells per well and incubated at 37 °C for 24 h. A scratch wound was created by gently scraping the cell monolayer using a sterile P200 micropipette tip. After washing the cells twice with DMEM to eliminate cell debris, they were treated with CA@FNPs, OLED irradiation, or by CA@FNPs plus OLED for durations ranging from 0 to 40 minutes. The control group was treated with DMEM solution including 1% penicillin–streptomycin. The healing of the cellular wound was evaluated at various time points (0, 12, 24, 48, and 72 hours) during a 72-hour incubation at 37 °C, using a microscope (KI-400, Korea Lab Tech, Korea). The measurements of the cellular wound gaps were computed with the aid of ImageJ software version 1.8.0 (National Institutes of Health, Bethesda, MD, USA).[14,75]

In vivo wound healing assay

Animals. Eight-week-old male BALB/c mice(20–25 g) purchased from Kosa Bio Inc. (Seongnam, Korea) were housed under a 12 h light/dark cycle at an ambient temperature of 22 ± 1 °C with 50% humidity. All experiments adhered to the guidelines of and were approved by the Institutional Animal Care and Use Committee of Chungbuk National University (CBNUA-25-0022-03).

Treatment of excisional wounds. The mice were randomly divided into four groups (n = 10 per group): Control, OLED, CA@FNPs and CA@FNPs plus OLED groups. After anesthesia with xylazine (5 mg kg^{-1}) and zoletil (30 mg kg^{-1}), an 8-mm circular wound was created on the dorsal area using a skin biopsy punch (29169, Acuderm inc, FL, USA). A silicone wound splint (476684; Grace Bio-Labs, OR, USA) was applied around the wound.[76] Mice in the OLED, CA@FNPs and CA@FNPs plus OLED groups were treated on the day of surgery and every five days thereafter. Wound healing was monitored on days 3, 5, 7, 10 and 14 after surgery. Wound areas were measured using the ImageJ software, and wound closure rates were calculated as follows: wound healing rate (%) = ((wound area on the given day)/(wound area on day 0)) × 100.

Histological evaluation. The dorsal skin of each mouse was fixed in 10% formalin for 24 h. The skin specimens were then embedded in paraffin and cut into 5 μm sections.[77] The skin sections were stained with hematoxylin and eosin (H&E) to examine epidermal thickness. The H&E-stained skin specimens were observed under a microscope (Leica DMi8, Leica, Wetzlar, Germany).

Western blot analysis. Total protein was isolated from dorsal skin tissue. Protein concentration was measured using the Bicinchoninic Acid Protein Assay kit (Pierce, IL, USA). Equal amounts of proteins were separated by acrylamide gel electrophoresis and transferred to PVDF membranes (Merck, Germany), which were then blocked with Tris-buffered saline containing Tween 20 (TBST) supplemented with 5% bovine serum albumin. The primary antibodies for claudin-1 (Santa Cruz Biotechnology, Texas, USA), VEGF-A (Cell Signaling Technology) ZO-1 (Santa Cruz), and β-Actin (Cell Signaling Technology) were probed onto the PVDF membrane overnight at 4 °C. All the primary antibodies were diluted 1 : 1000 using 5% BSA in TBS-T solution. Then, the secondary antibody, which was diluted at 1 : 2000 in the TBS-T solution, was incubated for 10 min at room temperature. To detect the target protein, the chemiluminescent substrate was reacted with the horseradish peroxidase conjugated with the secondary antibody for 1 min at room temperature. Target protein bands were observed and captured by Viber Fusion Solo S (Vilber Lourmat, France), and were quantified and normalized using Evolution-capt Edge software (Vilber Lourmat).

Author contributions

Kyung Cheol Choi, Daekyung Sung, Chan-Su Park, and Yongmin Jeon conceived the original concept and supervised the overall project. Hyejeong Yeon, Sohyeon Yu, Minhyeok Lee, and Sangwoo Kim designed and conducted the experiments, performed data analysis, and co-wrote the manuscript. Yongjin Park, Hye-Ryung Choi, Won Il Choi, and Chang-Hun Huh contributed to data interpretation, validation, and methodological analysis. All authors discussed the results, provided feedback, and approved the final version of the manuscript.

Conflicts of interest

There are no conflicts to declare.

Data availability

The data supporting this article have been included as part of the supplementary information (SI). Supplementary information is available. See DOI: https://doi.org/10.1039/d5mh02129d.

Acknowledgements

This work was supported by the National R&D Program through the National Research Foundation of Korea (NRF) funded by the Ministry of Science and ICT (2021M3C1C3097646).

Notes and references

1 B. R. Freedman, C. Hwang, S. Talbot, B. Hibler, S. Matoori and D. J. Mooney, *Sci. Adv.*, 2023, **9**, eade7007.
2 O. A. Peña and P. Martin, *Nat. Rev. Mol. Cell Biol.*, 2024, **25**, 599–616.
3 S. Yamakawa and K. Hayashida, *Burns Trauma*, 2019, **7**, 1–13.
4 D. Jhansi and M. Kola, *Fitoterapia*, 2019, **7**, 18–20.
5 A. M. Vargason, A. C. Anselmo and S. Mitragotri, *Nat. Biomed. Eng.*, 2021, **5**, 951–967.
6 G. Tiwari, R. Tiwari, S. Bannerjee, L. Bhati, S. Pandey, P. Pandey and B. Sriwastawa, *Int. J. Pharm. Invest.*, 2012, **2**, 2.

7 E. H. Cho, Y. W. Kim, J. Sim, H. Yeon, S. Baek, S. M. Jeong, J. Lee, Y. Jeon and K. C. Choi, *Mater. Horiz.*, 2025, 8862–8894.
8 C. Won, C. Kwon, K. Park, J. Seo and T. Lee, *Adv. Mater.*, 2021, **33**, e2005930.
9 A. Pandiyan, R. Vengudusamy, L. Veeramuthu, A. Muthuraman, Y. C. Wang, H. Lee, T. Zhou, C. R. Kao and C. C. Kuo, *Nano Energy*, 2025, **133**, 110426.
10 L. Veeramuthu, R. J. Weng, W. H. Chiang, A. Pandiyan, F. J. Liu, F. C. Liang, G. R. Kumar, H. Y. Hsu, Y. C. Chen, W. Y. Lin, Y. C. Tang, W. R. Lin, R. J. Chung, T. Zhou and C. C. Kuo, *Chem. Eng. J.*, 2024, **502**, 157752.
11 M. Venkatesan, J. Chandrasekar, Y. C. Hsu, T. W. Sun, P. Y. Li, X. T. King, M. A. Chung, R. J. Chung, W. Y. Lee, Y. Zhou, J. H. Lin and C. C. Kuo, Adv., *Sci.*, 2024, **11**, 2404019.
12 L. Veeramuthu, F. R. Liang, C. H. Chen, F. C. Liang, Y. T. Lai, Z. L. Yan, A. Pandiyan, C. T. Tsai, W. C. Chen, J. C. Lin, M. H. Chen, C. C. Chueh and C. C. Kuo, *ACS Appl. Mater. Interfaces*, 2025, **17**, 1782–1791.
13 M. J. Mitchell, M. M. Billingsley, R. M. Haley, M. E. Wechsler, N. A. Peppas and R. Langer, *Nat. Rev. Drug Discovery*, 2021, **20**, 101–124.
14 Y. Na, J. Woo, W. Il Choi, J. H. Lee, J. Hong and D. Sung, *Int. J. Pharm.*, 2021, **596**, 120205.
15 Y. Na, J. Woo, W. Il Choi and D. Sung, *Colloids Surf., B*, 2021, **200**, 111566.
16 S. Yu, M. Lee, D. Seo, H. Kim, C. S. Park and D. Sung, *Redox Biol.*, 2025, **84**, 103659.
17 H. Yu, R. Gao, Y. Liu, L. Fu, J. Zhou and L. Li, *Adv. Sci.*, 2024, **11**, 2306152.
18 Y. Yang, K. Long, Y. Chu, H. Lu, W. Wang and C. Zhan, *Adv. Funct. Mater.*, 2024, **34**, 2402975.
19 H. Chung, T. Dai, S. K. Sharma, Y. Y. Huang, J. D. Carroll and M. R. Hamblin, *Ann. Biomed. Eng.*, 2012, **40**, 516–533.
20 E. Giannakopoulos, A. Katopodi, M. Rallis, K. Politopoulos and E. Alexandratou, *J. Biophotonics*, 2024, **17**, e202400033.
21 D. P. Kuffler, *Regener. Med.*, 2016, **11**, 107–122.
22 Y. Park, H.-R. Choi, Y. Jeon, H. Kim, J. W. Shin, C.-H. Huh, K.-C. Park and K.-C. Choi, *Sci. Rep.*, 2022, **12**, 10935.
23 Y. Y. Huang, A. C. H. Chen, J. D. Carroll and M. R. Hamblin, *Dose-Response*, 2009, **7**, 358–383.
24 Y. Lee, H. Kim, N. Hong, J. C. Ahn and H. W. Kang, *Lasers Surg. Med.*, 2020, **52**, 276–285.
25 H. M. Panah, M. Abbasi, Z. Yazdi and M. Hayati, *J. Bodywork Mov. Ther.*, 2021, **27**, 705–709.
26 C. H. Kim, K. A. Cheong and A. Y. Lee, *J. Dermatol. Sci.*, 2013, **72**, 142–148.
27 S. Y. Lee, S. Jeon, Y. Woo Kwon, M. Kwon, M. Sung Kang, K.-Y. Seong, T.-E. Park, S. Yun Yang, D.-W. Han, S. Won Hong and K. Su, *Sci. Adv.*, 2022, **8**, eabn1646.
28 Y. Jeon, H. R. Choi, M. Lim, S. Choi, H. Kim, J. H. Kwon, K. C. Park and K. C. Choi, *Adv. Mater. Technol.*, 2018, **3**, 1700391.
29 S. Choi, Y. Jeon, J. H. Kwon, C. Ihm, S. Y. Kim and K. C. Choi, *Adv. Sci.*, 2022, **9**, 2204622.
30 Y. W. Kim, J. Y. Jeong, E. S. Cho, S. J. Kwon, J. H. Kwon, Y. J. Hwang and Y. Jeon, *Nano Res.*, 2025, **18**, 94907409.
31 J. Lee, C. Y. Gu, J. Chang, E. H. Cho, T. S. Kim and K. C. Choi, *npj Flexible Electron.*, 2024, **8**, 73.
32 J. Kim, H. Yeon, H. R. Choi, S. M. Park, C. H. Huh, K. C. Choi and D. K. Yoon, *Adv. Opt. Mater.*, 2024, **12**, 2400702.
33 H. Yeon, H. R. Choi, S. Yu, Y. Park, H. Kim, D. Sung, C. H. Huh and K. C. Choi, *J. Soc. Inf. Disp.*, 2025, **33**, 513–523.
34 Y. Jeon, H. R. Choi, J. H. Kwon, S. Choi, K. M. Nam, K. C. Park and K. C. Choi, *Light: Sci. Appl.*, 2019, **8**, 114.
35 H. Kim, H. R. Choi, Y. Park, Y. Jeon, H. S. Lee, E. G. Jeong, K. C. Park and K. C. Choi, *Adv. Mater. Interfaces*, 2021, **8**, 2100856.
36 S. Lee, H. J. Kim, J. H. Choi, H. J. Jang, H. B. Cho, H. R. Kim, J. Park, K. Soon Park and K. H. Park, *J. Controlled Release*, 2024, **368**, 756–767.
37 C. S. Linsley and B. M. Wu, *Ther. Delivery*, 2017, **8**, 89–107.
38 Y. Jeon, H. R. Choi, K. C. Park and K. C. Choi, *J. Soc. Inf. Disp.*, 2020, **28**, 324–332.
39 Y. Park, H. R. Choi, J. W. Shin, C. H. Huh and K. C. Choi, *J. Inf. Disp.*, 2023, 1–6.
40 E. H. Cho, H. R. Choi, Y. Park, S. Y. Jeong, Y. J. Song, Y. H. Hwang, J. Lee, Y. Chi, S. F. Wang, Y. Jeon, C. H. Huh and K. C. Choi, *ACS Appl. Mater. Interfaces*, 2023, **15**, 57415–57426.
41 J. H. Sim, J. Kwon, H. Chae, S.-B. Kim, H. Cho, W. Lee, S. Hee Kim, C.-W. Byun, S. Hahn, D. Hyun Park and S. Yoo, *Sci. Adv.*, 2023, **9**, eadh8619.
42 Y. Park, H.-R. Choi, H. Yeon, H. Lee, Y. Jung, J.-W. Shin, C.-H. Huh and K.-C. Choi, *Nano Lett.*, 2025, **25**, 13118–13127.
43 S. Lee, M. K. Kim, S. Kwon, J. C. Leong, B. Noh, J. Sim, E. G. Jeong, H. J. Lee and K. C. Choi, *Adv. Funct. Mater.*, 2025, **35**, 2420758.
44 D. Y. Baek, J. Heo, H. Kim, K. Kim, D. Han, Y. Jeon and S. Kim, SPIE-Intl. Soc. Optical Eng., 2024, p. 22.
45 Y. Jeon, I. Noh, Y. C. Seo, J. H. Han, Y. Park, E. H. Cho and K. C. Choi, *ACS Nano*, 2020, **14**, 15688–15699.
46 Y. Na, J. S. Lee, J. Woo, S. Ahn, E. Lee, W. Il Choi and D. Sung, *J. Mater. Chem. B*, 2020, **8**, 1906–1913.
47 A. Joorabloo and T. Liu, *Exploration*, 2024, **4**, 20230066.
48 Z. Quan, S. Wang, H. Xie, J. Zhang, R. Duan, M. Li and J. Zhang, *Small*, 2025, **21**, 2410031.
49 A. C.-H. Chen, Y.-Y. Huang, P. R. Arany and M. R. Hamblin, *in Mechanisms for Low-Light Therapy IV*, SPIE, 2009, vol. 7165, p. 716502.
50 Z. B. Yaralı Çevik, O. Karaman and N. Topaloğlu, *J. Photochem. Photobiol., B*, 2023, **238**, 112615.
51 M. Hunt, M. Torres, E. Bachar-Wikstrom and J. D. Wikstrom, *Commun. Biol.*, 2024, **7**, 1534.
52 E. Arribas-López, N. Zand, O. Ojo, M. J. Snowden and T. Kochhar, *Int. J. Environ. Res. Public Health*, 2022, **19**, 3266.
53 E. G. Jeong, Y. Jeon, S. H. Cho and K. C. Choi, *Energy Environ. Sci.*, 2019, **12**, 1878–1889.

54 N. Manfredi, C. Decavoli, C. L. Boldrini, C. Coluccini and A. Abbotto, *Energies*, 2020, **13**, 3937.
55 H. Ye and S. De, *Burns*, 2017, **43**, 909–932.
56 S. Kim, S. Yu, J. Kim, N. U. Khaliq, W. Il Choi, H. Kim and D. Sung, *Antioxidants*, 2023, **12**, 207.
57 N. M. Nazmi and N. M. Sarbon, *Food Res.*, 2020, **4**, 224–233.
58 H. Lee, J. Woo, D. Son, M. Kim, W. Il Choi and D. Sung, *Polymers*, 2020, **12**, 1–11.
59 V. Hmingthansanga, N. Singh, S. Banerjee, S. Manickam, R. Velayutham and S. Natesan, *Pharmaceutics*, 2022, **14**, 2818.
60 B. Latha and M. Babu, *Burns*, 2001, **27**, 309–317.
61 J. Xin, Z. Yang, S. Zhang, L. Sun, X. Wang, Y. Tang, Y. Xiao, H. Huang and W. Li, *J. Nanobiotechnol.*, 2024, **22**, 439.
62 T. R. Leonardo, J. Shi, D. Chen, H. M. Trivedi and L. Chen, *Int. J. Mol. Sci.*, 2020, **21**, 2966.
63 W. T. Kuo, M. A. Odenwald, J. R. Turner and L. Zuo, *Ann. N. Y. Acad. Sci.*, 2022, **1514**, 21–33.
64 C. A. O'Neill and D. Garrod, *Exp. Dermatol.*, 2011, **20**, 88–91.
65 J.-L. Guan, *Cell Migration: Developmental Methods and Protocols*, Totowa, NJ, USA, 2005.
66 H. Oh, E. Jeong, J. S. Lee, J. Kim, D. Lee, B. S. Kim, D. Sung, H. Koo, W. Il Choi and G. Tae, *Mater. Today Bio*, 2023, **22**, 100774.
67 Y. Xia, R. Chen, Y. Ke, Z. Xiang, Z. Ma, Q. Shi, F. I. Ataullakhanov and M. Panteleev, *Macromol. Chem. Phys.*, 2022, **223**, 1–9.
68 J. Li, W. Ke, L. Wang, M. Huang, W. Yin, P. Zhang, Q. Chen and Z. Ge, *J. Controlled Release*, 2016, **225**, 64–74.
69 D. Figueroa, M. Asaduzzaman and F. Young, *J. Pharmacol. Toxicol. Methods*, 2018, **94**, 26–33.
70 H. Yang, S. Yu, J. Kim, K. Baek, Y. R. Lee, H. S. Lee, W. Il Choi and D. Sung, *Pharmaceutics*, 2022, **14**, 521.
71 W. J. Shim, Y. K. Song, S. H. Hong and M. Jang, *Mar. Pollut. Bull.*, 2016, **113**, 469–476.
72 S. Küchler, M. R. Radowski, T. Blaschke, M. Dathe, J. Plendl, R. Haag, M. Schäfer-Korting and K. D. Kramer, *Eur. J. Pharm. Biopharm.*, 2009, **71**, 243–250.
73 S. A. El-Lakany, A. I. Abd-Elhamid, E. A. Kamoun, E. M. El-Fakharany, W. M. Samy and N. A. Elgindy, *Int. J. Nanomed.*, 2019, **14**, 8251–8270.
74 S. Yu, S. Kim, J. Kim, J. W. Kim, S. Y. Kim, B. Yeom, H. Kim, W. I. I. Choi and D. Sung, *Int. J. Nanomed.*, 2023, **18**, 4555–4565.
75 A. Gnerucci, P. Faraoni, E. Sereni and F. Ranaldi, *Math. Biosci.*, 2020, **330**, 108482.
76 X. Wang, J. Ge, E. E. Tredget and Y. Wu, *Nat. Protoc.*, 2013, **8**, 302–309.
77 W. H. Jang, S. Shim, T. Wang, Y. Yoon, W. S. Jang, J. K. Myung, S. Park and K. H. Kim, *Sci. Rep.*, 2016, **6**, 19216.